FRONTIERS OF PHYSICS

RESEARCH ARTICLE
Volume 19 / Issue 1 / 13201 / 2024

Two-dimensional polarized MoSSe/$MoTe_2$ van der Waals heterostructure: A polarization-tunable optoelectronic material

Fahhad Alsubaie[1], Munirah Muraykhan[1], Lei Zhang[1], Dongchen Qi[1], Ting Liao[2], Liangzhi Kou[2], Aijun Du[1,†], Cheng Tang[1,‡]

1 School of Chemistry and Physics, Centre for Materials Science, Queensland University of Technology, Brisbane, QLD 4001, Australia
2 School of Mechanical, Medical and Process Engineering, Queensland University of Technology, Brisbane, QLD 4001, Australia
Corresponding authors. E-mail: †aijun.du@qut.edu.au, ‡c21.tang@qut.edu.au
Received March 13, 2023; accepted July 4, 2023

ABSTRACT

Two-dimensional (2D) heterostructures have shown great potential in advanced photovoltaics due to their restrained carrier recombination, prolonged exciton lifetime and improved light absorption. Herein, a 2D polarized heterostructure is constructed between Janus MoSSe and $MoTe_2$ monolayers and is systematically investigated via first-principles calculations. Electronically, the valence band and conduction band of the MoSSe–$MoTe_2$ (MoSeS–$MoTe_2$) are contributed by $MoTe_2$ and MoSSe layers, respectively, and its bandgap is 0.71 (0.03) eV. A built-in electric field pointing from $MoTe_2$ to MoSSe layers appears at the interface of heterostructures due to the interlayer carrier redistribution. Notably, the band alignment and built-in electric field make it a direct z-scheme heterostructure, benefiting the separation of photogenerated electron-hole pairs. Besides, the electronic structure and interlayer carrier reconstruction can be readily controlled by reversing the electric polarization of the MoSSe layer. Furthermore, the light absorption of the MoSSe/$MoTe_2$ heterostructure is also improved in comparison with the separated monolayers. Consequently, in this work, a new z-scheme polarized heterostructure with polarization-controllable optoelectronic properties is designed for highly efficient optoelectronics.

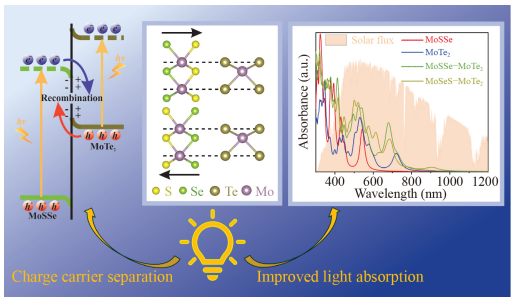

Keywords MoSSe/$MoTe_2$, photovoltaics, ferroelectric heterostructure

1 Introduction

Solar power has been recognised as an essential green energy resource to replace the conventional fossil energy, which attracts considerable attention for advanced applications, involving solar photovoltaics, solar heating system and solar thermoelectric devices [1–4]. Among them, photovoltaics have been developed as a mature technology that converts energy from the sunlight into a flow of electrons by collecting excited electrons or holes at counter electrodes. Currently, the highest power conversion efficiency of the photovoltaic solar system

Higher Education Press

https://doi.org/10.1007/s11467-023-1330-2

reaches 25% at an organometallic stabilizing perovskite [5]. However, the costs, stability and toxicity of a perovskite-based devices still limit its possibility for practical large-scale production [6]. Therefore, it is still of great significance to design a stable non-perovskite system with suitable bandgap and large charge carrier separation for advanced photovoltaic applications.

Two-dimensional (2D) semiconducting materials exhibits great potentials on photovoltaic applications, due to its large specific surface area, highly-efficient light absorption, ultrahigh charge carrier transportation [7]. Significantly, these atomically thin materials possess excellent flexibility in terms of tuning their physicochemical properties [8–10]. Among them, 2D transition metal dichalcogenides (TMDs) with a sandwiched MX_2 (M = transition metals and X = S, Se and/or Te) stoichiometry possesses diverse electronic/optical characters [11]. Especially, semiconducting 2H-TMDs, such as MoX_2 and WX_2 nanosheets, with stimuli-controllable electronic structures has shown great potentials on photoelectrochemical solar energy conversion [12]. Furthermore, the development of techniques on heterostructure engineering remarkably enhance the efficiency of light absorption and excited charge carrier separation by forming the proper band alignment [13–15]. The photogenerated electrons or holes can accumulate at different components of heterostructures due to the induced built-in electric fields in type-II or z-scheme paths [16–18]. Thus, the construction of 2D heterostructures with proper band alignment can efficiently improve the performance of photovoltaic/optoelectronic nanodevices.

Since the in-plane electric polarization can lead to the emergence of a spontaneous photovoltaic effect in WSe_2/black phosphorus heterostructure [19], it is highly expected to achieve the polarization-controlled photovoltaic performance by constructing the polarized heterostructure [20]. Recently, 2D Janus TMDs (MXY, X ≠ Y) with asymmetric geometry have been successfully fabricated by using the chemical vapor deposition (CVD) approach, attracting considerable attention for its intriguing optoelectronic features [21–23]. An inherent electric polarization is generated from the structural asymmetry, which is beneficial to the separation of excited electron–hole pairs by limiting charge carrier recombination [24]. The carrier mobility of photogenerated electrons and holes could be completely different in Janus TMDs [25–28]. Besides, the lattice parameters of MXY generally keep similar to the MX_2 containing the same transition metals [29]. Therefore, MXY is a promising materials platform to build polarized heterostructures with MX_2 monolayers. The superior photovoltaic/optoelectronic performance is also expected to be achieved in MXY/MX_2 heterostructures.

2D Janus MoSSe and $MoTe_2$ possess excellent stability and appropriate bandgap of around 2.0 eV [21, 30]. However, their optoelectronic application is still limited by the short lifetime excited charge carriers. To improve the photo response character and prolong the lifetime of excitons, in this work, we constructed a heterostructure based on the Janus MoSSe and $MoTe_2$ monolayers and systematically investigated its polarization-controlled optoelectronic properties. The negative formation energy indicates the thermal stability of the constructed heterostructures (MoSSe–$MoTe_2$ and MoSeS–$MoTe_2$). Electronically, the bandgaps of MoSSe–$MoTe_2$ and MoSeS–$MoTe_2$ heterostructures are remarkably reduced to 0.71 and 0.03 eV, respectively, due to the formed z-scheme band alignment between the monolayers. Notably, the vertical polarization induced by MoSSe monolayer will further trigger the interlayer charge redistribution, suggesting the polarization-controlled charge transfer and built-in electric fields. Besides, the light absorption is also improved after forming the heterostructure, especially in the visible-light region. The proper band alignment and polarization-controllable feature of MoSSe/$MoTe_2$ heterostructures provide a promising platform for advanced optoelectronic nanodevices.

2 Computational methods

All calculations were performed based on density functional theory (DFT) method, as implemented in Vienna Ab-initio Simulation Package (VASP) [31–33]. The projected augmented wave (PAW) [34] method was used to describe the ion–electron correlation, while the Perdew–Burke–Ernzerhof generalized gradient approximation (PBE-GGA) [35] functional was adopted. The energy cut-off was set to be 500 eV, and the first Brillouin zone (BZ) was sampled by a 21 × 21 × 1 Gamma-centred k-mesh [36]. To prevent the adjacent interaction between the periodic layers, a vacuum thickness of 20 Å was used. Since the bandgap would be underestimated by the PBE-GGA functional, the Heyd–Scuseria–Ernzerhof hybrid functional (HSE06) was applied to calculate the electronic properties. Besides, the DFT-D3 method was adopted to correct the long-range van der Waals interaction [37]. Moreover, all structures were fully relaxed until the energy and force on each atom converge to 10^{-6} eV and 0.001 eV/Å.

The optical absorption can be calculated by

$$\alpha(\omega) = \frac{\sqrt{2\omega}}{c}\{[\varepsilon_1^2(\omega) + \varepsilon_2^2(\omega)]^{1/2} - \varepsilon_1(\omega)\}^{1/2},$$

where $\varepsilon_1(\omega)$ and $\varepsilon_2(\omega)$ represent the real and imaginary parts of the complex dielectric function, respectively, which was obtained by using the vaspkit code [38].

3 Results and discussion

The optimized MoSSe and $MoTe_2$ monolayers are in the

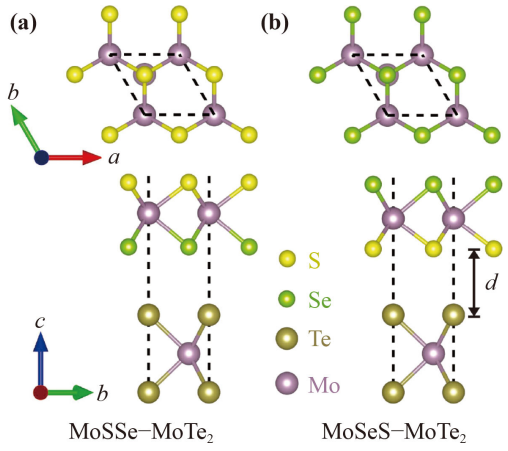

Fig. 1 Top and side views of optimized geometries for **(a)** MoSSe–$MoTe_2$ and **(b)** MoSeS–$MoTe_2$ heterostructures, respectively. Yellow, green, brown and purple spheres represent sulfer, selenium, titanium and molybdenum atoms, respectively.

space group of $P3m1$ with the lattice parameters of 3.23 and 3.52 Å, respectively, close to previous experimental researches [39, 40]. Accordingly, the MoSSe/$MoTe_2$ heterostructure is constructed between the unit cell of each layer with the lattice mismatch of around 8%. As shown in Fig. 1, two heterostructures with reversed electric polarization of MoSSe layer are presented as MoSSe–$MoTe_2$ and MoSeS–$MoTe_2$, forming the Se/Te and S/Te interface, respectively. The lattice parameter of MoSSe/$MoTe_2$ heterostructure is calculated to be 3.36 Å, suggesting a tiny tensile (compression) in the MoSSe ($MoTe_2$) layer. Besides, the interlayer distances of MoSSe–$MoTe_2$ and MoSeS–$MoTe_2$ are 3.31 Å and 3.18 Å (see Table 1), indicating the polarization-controlled interlayer interaction. To evaluate the thermal stability of heterostructure, the formation energy (E_f) is computed by, $E_f = E_H - E_{MoTe_2} - E_{MoSSe}$, where E_H, E_{MoTe_2} and E_{MoSSe} represent total energies of the heterostructure, $MoTe_2$ and MoSSe monolayer, respectively. As shown in Table 1, E_f is calculated to be –8.92 meV for the MoSSe–$MoTe_2$ heterostructure and –6.77 meV for the MoSeS–$MoTe_2$, indicating that the formation of the heterostructure is energetically favourite.

To understand the behaviour of the photoelectric response of constructed polarized heterostructure, we next investigated their electronic characters. All the band structures are calculated based on the hybrid functional (HSE06) to obtain a more accurate bandgap. As shown in Fig. 2, MoSSe and $MoTe_2$ monolayers are direct semiconductors (at K point) with the bandgap of 2.10 and 1.60 eV, respectively, close to the experimental values (Table 1) [39, 40]. Then, we calculated the electrostatic potential of the separated layers along the z direction [Fig. 2(c)]. Due to the polarized structure, MoSSe monolayer has two work functions, namely –6.40 eV for S surface and –5.63 eV for Se surface. Besides, the work function for $MoTe_2$ monolayer is calculated to be –5.11 eV, slightly higher than those of MoSSe monolayer. When forming the heterostructure, different work functions will have impact on the interfacial carrier redistribution and built-in electric field, thus, manipulate its electronic properties. Figure 2(d) presents the potentials of valence band maximum (VBM) and conduction band minimum (CBM) of MoSSe and $MoTe_2$ monolayers. The gap between VBM of $MoTe_2$ layer and CBM of MoSSe layer narrows for S/Te interface of the MoSeS–$MoTe_2$ heterostructure [0.03 eV as detailed in Fig. S1 of the Electronic Supplementary Materials (ESM)] in comparison with Se/Te interface of the MoSSe–$MoTe_2$ (0.71 eV), due to the large difference on interlayer electrostatic potentials of S–Te and Se–Te of the polarized heterostructure. This is also confirmed by the orbital-resolved band structure and band decomposed charge density of the heterostructures, as given in Figs. 2(e) and (f). In both MoSSe–$MoTe_2$ and MoSeS–$MoTe_2$ heterostructures, the valence band (VB) is mainly contributed by Mo orbitals of $MoTe_2$ layer, while the conduction band (CB) originates from the Mo orbitals of MoSSe layer. The location of VBM and CBM in MoSSe/$MoTe_2$ heterostructure meets the requirement of type-II or z-scheme band alignment, which remains to be further investigated by considering the interlayer charge carrier redistribution.

The charge density difference ($\Delta\rho$) can be given by $\Delta_\rho = \rho_H - \rho_{MoTe_2} - \rho_{MoSSe}$, where ρ_H, ρ_{MoTe_2} and ρ_{MoSSe} are calculated charge densities of heterostructure, $MoTe_2$ and MoSSe monolayers, respectively. As plotted in Fig. 3, the electrons are mainly depleted from the $MoTe_2$ layer, while accumulated at Se or S atomic layer in both heterostructures, indicating an interlayer electron transfer from Te surface to S or Se surface. Bader analysis confirms that $0.03e$ and $0.05e$ electrons transfer occurs

Table 1 Lattice constants (Å) and bandgaps (eV) (HSE functional) for MoSSe and $MoTe_2$ monolayer and MoSSe–$MoTe_2$ and MoSeS–$MoTe_2$ heterostructures. Formation energy (meV) and interlayer distance (Å) of heterostructures.

	Lattice constant	Bandgap (This work)	Bandgap (exp)	Formation energy	Interlayer distance
MoSSe	3.23	2.10	1.68 [40]	–	–
$MoTe_2$	3.52	1.60	1.10 [39]	–	–
MoSSe–$MoTe_2$	3.36	0.71	–	–8.92	3.31
MoSeS–$MoTe_2$	3.36	0.03	–	–6.77	3.18

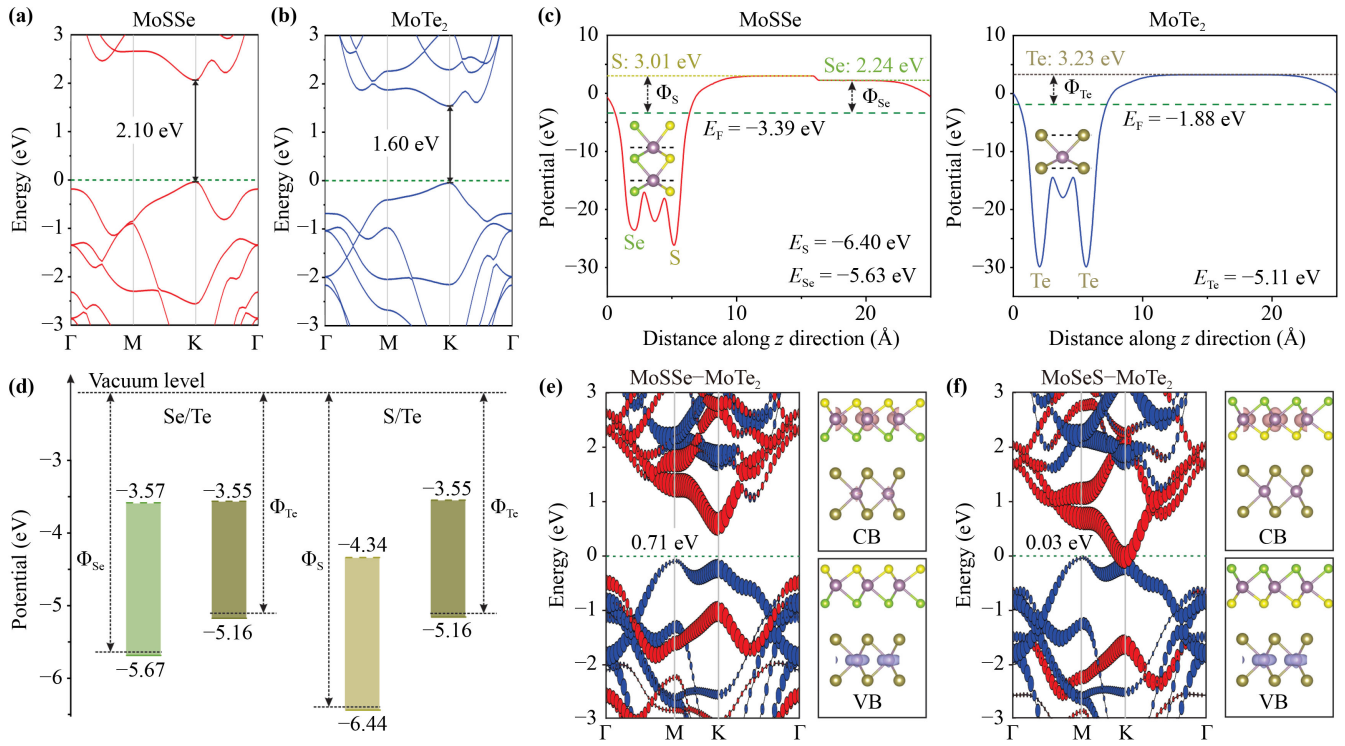

Fig. 2 **(a, b)** Band structures of MoSSe and $MoTe_2$ monolayers. **(c)** Electrostatic potential of MoSSe and $MoTe_2$ monolayers, respectively. The dipole correction is considered in these calculations. **(d)** Diagram illustration of band alignment of MoSSe–$MoTe_2$ and MoSeS–$MoTe_2$ heterostructures with interface of Se/Te and S/Te, respectively. Φ_x (x = S, Se and Te) represent the work functions estimated in (c) with x atomic surface. The potentials of valence (VB) and conduction (CB) bands are marked in the figure. **(e, f)** Orbital-resolved band structures and charge densities (iso-value of 0.012 e/Å^3) of VB and CB of MoSSe–$MoTe_2$ and MoSeS–$MoTe_2$ heterostructures, respectively. Red and Blue lines represent the contribution of orbitals from MoSSe and $MoTe_2$ layers, respectively.

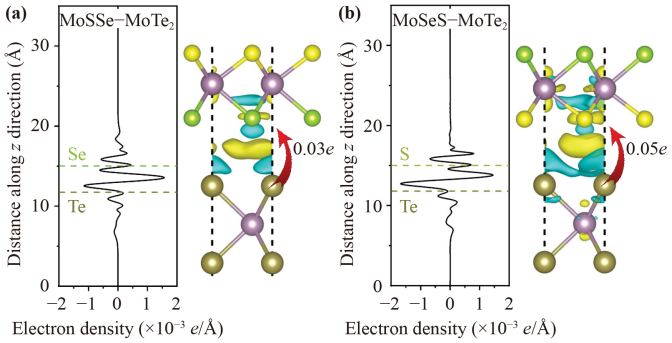

Fig. 3 Plane-averaged potential and charge density differences (iso-value of 0.0002 e/Å^3) for **(a)** MoSSe–$MoTe_2$ and **(b)** MoSeS–$MoTe_2$ heterostructures, respectively. Yellow and cyan area represent electron accumulation and depletion, respectively.

at the interface of MoSSe–$MoTe_2$ and MoSeS–$MoTe_2$ heterostructures, respectively. Obviously, the interlayer charge distribution of a polarized heterostructure determines by both the electric polarization of the MoSSe and the electronegativity between the surface atoms, which also has impacts on the transportation of the excited electrons and holes [25]. Since the electronegativity of Te atom is lower than that of S or Se atom, the direction of the electron transfer in such a heterostructure cannot be changed by the reversal of the electric polarization of MoSSe.

The interlayer electron transfer in MoSSe/$MoTe_2$ heterostructure gives rise to an electrostatic difference at the interface (Fig. S2 of the ESM), suggesting a built-in electric field pointing from the $MoTe_2$ layer to MoSSe layer. The effective electric potential difference of the heterostructure is given in Fig. 4 by subtracting the potential of MoSSe and $MoTe_2$ layers from the MoSSe/$MoTe_2$ heterostructure. Accordingly, the built-in electric field ($E_{\text{built-in}}$) at the interface can be obtained by $E_{\text{built-in}} = \frac{1}{e}\frac{\mathrm{d}V_{2-1}}{\mathrm{d}z}$, where $\mathrm{d}V_{2-1}$ is the potential difference of two interfacial layers, and $\mathrm{d}z$ represents the interlayer distance. Therefore, the calculated $E_{\text{built-in}}$ is 0.11 and 0.16 V/Å for MoSSe–$MoTe_2$ and MoSeS–$MoTe_2$ heterostructures, respectively, relying on the polarization-manipulated interlayer interaction [41, 42]. Such built-in electric field will also have impact on the transport of photogenerated electrons and holes. Consequently, excited holes of the $MoTe_2$ layer are allowed to transfer at the interface, as is the transport of excited electrons

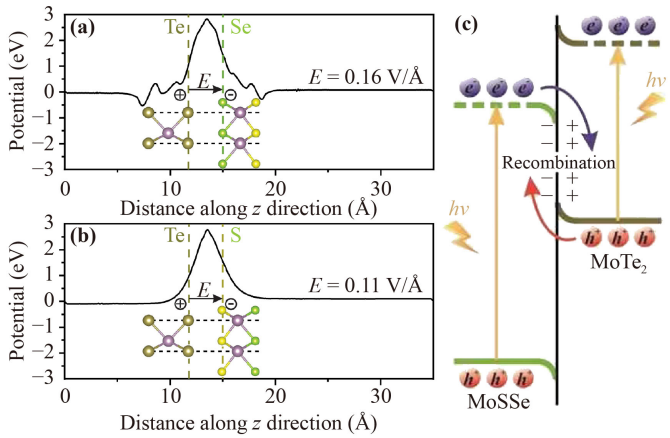

Fig. 4 Electrostatic potential difference of **(a)** MoSSe–$MoTe_2$ and **(b)** MoSeS–$MoTe_2$ heterostructures. The calculated built-in electric fields of Se/Te and S/Te interface are given in the figure, respectively. **(c)** Z-Scheme type of band alignment in MoSSe–$MoTe_2$ heterostructure.

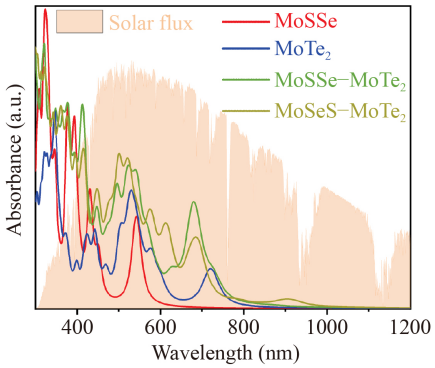

Fig. 5 Light absorption between 300 nm and 1200 nm for MoSSe and $MoTe_2$ monolayers and MoSSe–$MoTe_2$ and MoSeS–$MoTe_2$ heterostructures. The incident AM 1.5G Solar flux is plotted as a reference.

of the MoSSe layer, as illustrated in Fig. 4(c). It indicates the charge carrier recombination at both Te/Se and Te/S interface. However, excited electrons of the $MoTe_2$ and holes of the MoSSe layer are forbidden to transport at the interface. Thus, the depletion of excited holes (electrons) of the $MoTe_2$ (MoSSe) layer benefits to prolong the lifetime of its excited electrons (holes), achieving the separation of the photogenerated charge carriers. This mechanism of photogenerated charge carrier separation in MoSSe/$MoTe_2$ heterostructures belongs to the direct z-scheme band alignment.

Finally, excellent light absorption is also critical for highly efficient optoelectronic applications, and here we investigated the optical properties of the MoSSe/$MoTe_2$ heterostructure. The optical absorption spectra (from 300 nm to 1200 nm) of MoSSe and $MoTe_2$ monolayers as well as MoSSe–$MoTe_2$ and MoSeS–$MoTe_2$ heterostructures are shown in Fig. 5. Clearly, the absorption performance of the $MoTe_2$ monolayer is better than that of MoSSe layer corresponding to their bandgap. After forming the MoSSe/$MoTe_2$ heterostructure, the absorption strength significantly improved compared to the separated layers, especially at the visible light region (400–750 nm), due to the interfacial interaction. The peaks observed at 450, 600 and 700 nm of MoSSe/$MoTe_2$ heterostructure correspond well with the absorption peaks of single-layer MoSSe and $MoTe_2$, respectively, indicating a red or blue shift for their absorption peaks after forming the heterostructure. Such a shift is mainly due to the regulation of the bandgap caused by interlayer charge redistribution when forming the polarized heterostructure. Notably, a new absorption peak appears at around 900 nm in the MoSeS–$MoTe_2$ heterostructure, ascribing to the interlayer optical transition. These indicate an enhanced efficiency of solar light absorption via heterostructure engineering.

4 Conclusions

In conclusion, by using the first-principles calculation, we investigated a new z-scheme 2D polarized heterostructure (MoSSe/$MoTe_2$) with intriguing electronic and optical properties, rendering them potential materials platform for advanced optoelectronic applications. The existence of inherent electric polarization in the Janus MoSSe monolayer endows the heterostructure with the polarization-controlled optoelectronic response. The bandgap of the MoSSe–$MoTe_2$ is 0.71 eV, while it changes to 0.03 eV by reversing the polarization. Meanwhile, the interlayer electron transfer, built-in electric field, and light absorption are also various with the different polarization. Most importantly, the MoSSe/$MoTe_2$ heterostructure possesses z-scheme band alignment, mainly due to the contribution of its VB and CB and the direction of built-in electric field. The excited holes in the $MoTe_2$ layer can easily recombine with the excited electrons in the MoSSe layer, as a result, the photogenerated holes and electrons will remain in the MoSSe and $MoTe_2$ layer, respectively. Furthermore, the light absorption is also improved by forming the heterostructure compared to the separated layers. The improved performance on photogenerated carrier separation and light absorption makes the polarized MoSSe/$MoTe_2$ heterostructure a promising candidate for optoelectronic nanodevices.

Declarations The authors declare that they have no competing interests and there are no conflicts.

Electronic supplementary materials The online version contains supplementary material available at https://doi.org/10.1007/s11467-023-1330-2 and https://journal.hep.com.cn/fop/EN/10.1007/s11467-023-1330-2.

Acknowledgements The authors acknowledge grants of high-performance computing resources provided by NCI National Facility

and the Pawsey Supercomputing Centre through the National Computational Merit Allocation Scheme supported by Queensland University of Technology, the Australian Government and the Government of Western Australia. A.D. also greatly appreciates the financial support of the Australian Research Council under Discovery Projects DP210100721 and DP210100331.

References

1. S. Das, D. Pandey, J. Thomas, and T. Roy, The role of graphene and other 2D materials in solar photovoltaics, *Adv. Mater.* 31(1), 1802722 (2019)
2. Q. Li, X. Li, S. Wageh, A. A. Al-Ghamdi, and J. Yu, CdS/graphene nanocomposite photocatalysts, *Adv. Energy Mater.* 5(14), 1500010 (2015)
3. C. Han, Q. Sun, Z. Li, and S. X. Dou, Thermoelectric enhancement of different kinds of metal chalcogenides, *Adv. Energy Mater.* 6(15), 1600498 (2016)
4. Z. Liu, S. P. Lau, and F. Yan, Functionalized graphene and other two-dimensional materials for photovoltaic devices: Device design and processing, *Chem. Soc. Rev.* 44(15), 5638 (2015)
5. Z. Li, B. Li, X. Wu, S. A. Sheppard, S. Zhang, D. Gao, N. J. Long, and Z. Zhu, Organometallic-functionalized interfaces for highly efficient inverted perovskite solar cells, *Science* 376(6591), 416 (2022)
6. J. Ren, P. Bi, J. Zhang, J. Liu, J. Wang, Y. Xu, Z. Wei, S. Zhang, and J. Hou, Molecular design revitalizes the low-cost PTV-polymer for highly efficient organic solar cells, *Natl. Sci. Rev.* 8(8), nwab031 (2021)
7. C. Tang, L. Zhang, C. Zhang, J. MacLeod, K. K. Ostrikov, and A. Du, Highly stable two-dimensional gold selenide with large in-plane anisotropy and ultrahigh carrier mobility, *Nanoscale Horiz.* 5(2), 366 (2020)
8. C. H. Lee, G. H. Lee, A. M. Van Der Zande, W. Chen, Y. Li, M. Han, X. Cui, G. Arefe, C. Nuckolls, T. F. Heinz, J. Guo, J. Hone, and P. Kim, Atomically thin p–n junctions with van der Waals heterointerfaces, *Nat. Nanotechnol.* 9(9), 676 (2014)
9. X. Gu, W. Cui, H. Li, Z. Wu, Z. Zeng, S. T. Lee, H. Zhang, and B. Sun, A solution-processed hole extraction layer made from ultrathin MoS_2 nanosheets for efficient organic solar cells, *Adv. Energy Mater.* 3(10), 1262 (2013)
10. C. Tang, F. Ma, C. Zhang, Y. Jiao, S. K. Matta, K. Ostrikov, and A. Du, 2D boron dichalcogenides from the substitution of Mo with ionic B_2 pair in MoX_2 (X = S, Se and Te): High stability, large excitonic effect and high charge carrier mobility, *J. Mater. Chem. C* 7(6), 1651 (2019)
11. J. A. Wilson and A. Yoffe, The transition metal dichalcogenides discussion and interpretation of the observed optical, electrical and structural properties, *Adv. Phys.* 18(73), 193 (1969)
12. A. Splendiani, L. Sun, Y. Zhang, T. Li, J. Kim, C. Y. Chim, G. Galli, and F. Wang, Emerging photoluminescence in monolayer MoS_2, *Nano Lett.* 10(4), 1271 (2010)
13. C. Li, Q. Cao, F. Wang, Y. Xiao, Y. Li, J. J. Delaunay, and H. Zhu, Engineering graphene and TMDs based van der Waals heterostructures for photovoltaic and photoelectrochemical solar energy conversion, *Chem. Soc. Rev.* 47(13), 4981 (2018)
14. Y. Kim, S. Lee, J. G. Song, K. Y. Ko, W. J. Woo, S. W. Lee, M. Park, H. Lee, Z. Lee, H. Choi, W. H. Kim, J. Park, and H. Kim, 2D transition metal dichalcogenide heterostructures for p- and n-type photovoltaic self-powered gas sensor, *Adv. Funct. Mater.* 30(43), 2003360 (2020)
15. L. Britnell, R. M. Ribeiro, A. Eckmann, R. Jalil, B. D. Belle, A. Mishchenko, Y. J. Kim, R. V. Gorbachev, T. Georgiou, S. V. Morozov, A. N. Grigorenko, A. K. Geim, C. Casiraghi, A. H. C. Neto, and K. S. Novoselov, Strong light–matter interactions in heterostructures of atomically thin films, *Science* 340(6138), 1311 (2013)
16. M. Baranowski, A. Surrente, L. Klopotowski, J. M. Urban, N. Zhang, D. K. Maude, K. Wiwatowski, S. Mackowski, Y. C. Kung, D. Dumcenco, A. Kis, and P. Plochocka, Probing the interlayer exciton physics in a $MoS_2/MoSe_2/MoS_2$ van der Waals heterostructure, *Nano Lett.* 17(10), 6360 (2017)
17. X. Zheng, Y. Wei, J. Liu, S. Wang, J. Shi, H. Yang, G. Peng, C. Deng, W. Luo, Y. Zhao, Y. Li, K. Sun, W. Wan, H. Xie, Y. Gao, X. Zhang, and H. Huang, A homogeneous p–n junction diode by selective doping of few layer $MoSe_2$ using ultraviolet ozone for high-performance photovoltaic devices, *Nanoscale* 11(28), 13469 (2019)
18. K. Zhang, T. Zhang, G. Cheng, T. Li, S. Wang, W. Wei, X. Zhou, W. Yu, Y. Sun, P. Wang, D. Zhang, C. Zeng, X. Wang, W. Hu, H. J. Fan, G. Shen, X. Chen, X. Duan, K. Chang, and N. Dai, Interlayer transition and infrared photodetection in atomically thin type-II $MoTe_2/MoS_2$ van der Waals heterostructures, *ACS Nano* 10(3), 3852 (2016)
19. T. Akamatsu, T. Ideue, L. Zhou, Y. Dong, S. Kitamura, M. Yoshii, D. Yang, M. Onga, Y. Nakagawa, K. Watanabe, T. Taniguchi, J. Laurienzo, J. Huang, Z. Ye, T. Morimoto, H. Yuan, and Y. Iwasa, A van der Waals interface that creates in-plane polarization and a spontaneous photovoltaic effect, *Science* 372(6537), 68 (2021)
20. K. Zhang, Y. Guo, Q. Ji, A. Y. Lu, C. Su, H. Wang, A. A. Puretzky, D. B. Geohegan, X. Qian, S. Fang, E. Kaxiras, J. Kong, and S. Huang, Enhancement of van der Waals interlayer coupling through polar Janus MoSSe, *J. Am. Chem. Soc.* 142(41), 17499 (2020)
21. J. Zhang, S. Jia, I. Kholmanov, L. Dong, D. Er, W. Chen, H. Guo, Z. Jin, V. B. Shenoy, L. Shi, and J. Lou, Janus monolayer transition-metal dichalcogenides, *ACS Nano* 11(8), 8192 (2017)
22. X. Tang and L. Kou, 2D Janus transition metal dichalcogenides: Properties and applications, *Phys. Status Solidi B* 259(4), 2100562 (2022) (b)
23. D. Wijethunge, L. Zhang, C. Tang, and A. Du, Tuning band alignment and optical properties of 2D van der Waals heterostructure via ferroelectric polarization switching, *Front. Phys.* 15(6), 63504 (2020)
24. Y. Wang, F. Wang, Z. Wang, J. Wang, J. Yang, Y. Yao, N. Li, M. G. Sendeku, X. Zhan, and C. Shan, Reconfigurable photovoltaic effect for optoelectronic artificial synapse based on ferroelectric p–n junction, *Nano Res.* 14, 4328 (2021)

25. C. Xia, W. Xiong, J. Du, T. Wang, Y. Peng, and J. Li, Universality of electronic characteristics and photocatalyst applications in the two-dimensional Janus transition metal dichalcogenides, *Phys. Rev. B* 98(16), 165424 (2018)
26. M. J. Varjovi, M. Yagmurcukardes, F. M. Peeters, and E. Durgun, Janus two-dimensional transition metal dichalcogenide oxides: First-principles investigation of WXO monolayers with X = S, Se, and Te, *Phys. Rev. B* 103(19), 195438 (2021)
27. X. Wang, P. Wang, J. Wang, W. Hu, X. Zhou, N. Guo, H. Huang, S. Sun, H. Shen, T. Lin, M. Tang, L. Liao, A. Jiang, J. Sun, X. Meng, X. Chen, W. Lu, and J. Chu, Ultrasensitive and broadband MoS_2 photodetector driven by ferroelectrics, *Adv. Mater.* 27(42), 6575 (2015)
28. W. J. Yin, X. L. Zeng, B. Wen, Q. X. Ge, Y. Xu, G. Teobaldi, and L. M. Liu, The unique carrier mobility of Janus MoSSe/GaN heterostructures, *Front. Phys.* 16(3), 33501 (2021)
29. M. Absor, A. Ulil, I. Santoso, H. Harsojo, K. Abraha, H. Kotaka, F. Ishii, and M. Saito, Polarity tuning of spin–orbit-induced spin splitting in two-dimensional transition metal dichalcogenides, *J. Appl. Phys.* 122(15), 153905 (2017)
30. Y. Wang, J. Xiao, H. Zhu, Y. Li, Y. Alsaid, K. Y. Fong, Y. Zhou, S. Wang, W. Shi, Y. Wang, A. Zettl, E. J. Reed, and X. Zhang, Structural phase transition in monolayer $MoTe_2$ driven by electrostatic doping, *Nature* 550(7677), 487 (2017)
31. G. Kresse and J. Furthmüller, Efficiency of *ab-initio* total energy calculations for metals and semiconductors using a plane-wave basis set, *Comput. Mater. Sci.* 6(1), 15 (1996)
32. G. Kresse and J. Furthmüller, Efficient iterative schemes for *ab initio* total-energy calculations using a plane-wave basis set, *Phys. Rev. B* 54(16), 11169 (1996)
33. G. Kresse and J. Hafner, *Ab initio* molecular-dynamics simulation of the liquid-metal–amorphous-semiconductor transition in germanium, *Phys. Rev. B* 49(20), 14251 (1994)
34. G. Kresse and D. Joubert, From ultrasoft pseudopotentials to the projector augmented-wave method, *Phys. Rev. B* 59(3), 1758 (1999)
35. J. P. Perdew, K. Burke, and M. Ernzerhof, Generalized gradient approximation made simple, *Phys. Rev. Lett.* 77(18), 3865 (1996)
36. H. J. Monkhorst and J. D. Pack, Special points for Brillouin-zone integrations, *Phys. Rev. B* 13(12), 5188 (1976)
37. S. Grimme, J. Antony, S. Ehrlich, and H. Krieg, A consistent and accurate *ab initio* parametrization of density functional dispersion correction (DFT-D) for the 94 elements H–Pu, *J. Chem. Phys.* 132(15), 154104 (2010)
38. V. Wang, N. Xu, J. C. Liu, G. Tang, and W. T. Geng, VASPKIT: A user-friendly interface facilitating high-throughput computing and analysis using VASP code, *Comput. Phys. Commun.* 267, 108033 (2021)
39. C. Ruppert, O. B. Aslan, and T. F. Heinz, Optical properties and band gap of single- and few-layer $MoTe_2$ crystals, *Nano Lett.* 14(11), 6231 (2014)
40. A. Y. Lu, H. Zhu, J. Xiao, C. P. Chuu, Y. Han, M. H. Chiu, C. C. Cheng, C. W. Yang, K. H. Wei, Y. Yang, Y. Wang, D. Sokaras, D. Nordlund, P. Yang, D. A. Muller, M. Y. Chou, X. Zhang, and L. J. Li, Janus monolayers of transition metal dichalcogenides, *Nat. Nanotechnol.* 12(8), 744 (2017)
41. C. Zhang, Y. Jiao, T. He, S. Bottle, T. Frauenheim, and A. Du, Predicting two-dimensional C_3B/C_3N van der Waals p–n heterojunction with strong interlayer electron coupling and enhanced photocurrent, *J. Phys. Chem. Lett.* 9(4), 858 (2018)
42. C. Tang, L. Zhang, and A. Du, Tunable magnetic anisotropy in 2D magnets via molecular adsorption, *J. Mater. Chem. C* 8(42), 14948 (2020)